

Crystal or Glass? Chemical and Crystallographic Factors in Amorphization of Molecular Materials.

Nathan W. Fenwick, Richard Telford, Richard D. Bowen, Colin C. Seaton*.

School of Chemistry and Biosciences, University of Bradford, Richmond Road, Bradford, UK, BD7 1DP.

ABSTRACT: The creation of long-lived amorphous phases has potential applications in numerous fields, for example the instability of the amorphous phase leads to higher solubility of pharmaceutical phases often leading to higher bioavailability. The rate of recrystallisation of an amorphous phase offers the key limitation on the application of many such phases, yet understanding the energetic and structural factors that control the stability of molecular amorphous phases is limited with, empirical classifications based on thermal analysis used to identify materials. From a set of molecularly related benzanilides, examples of all three classes have been identified allowing use of crystal structural analysis, Raman spectroscopy and energetic calculations to determine the structural factors playing a role in the different stabilities. While the behavior of most systems reflects the relative energy of the crystalline phase to the amorphous, kinetic factors based on whether a NH...O=C hydrogen bond is present in the crystalline phase plays a key role in stabilizing the amorphous phase as the loss of this bond reduces the conversion rate. In contrast, systems without this bond display fast recrystallisation due to the greater structural similarity between the amorphous and crystalline phases.

INTRODUCTION

A given compound can be present in a range of solid forms including different crystal structures (polymorphism),¹ complexed with other compounds (co-crystals, salts, hydrates and solvates)² or as an amorphous phase with no long-range order.³ The choice of solid-state form plays a key role in controlling the physicochemical properties. Amorphous materials are higher energy states than crystalline phases and so will display higher solubilities which can be beneficial for pharmaceutical materials.⁴ However, the amorphous state is inherently unstable compared to the crystalline form and so may spontaneously recrystallize.⁵ Thus, understanding the chemical and crystallographic factors that control the stability of a given crystal phase is vital to develop the ability to predict and design phases with increased amorphous stability.

Studies into what makes a good amorphous former have been carried out for both organic and inorganic materials.⁶ An empirical crystallization classification based on the thermal behavior recorded by heat/cool/heat cycle by differential scanning calorimetry (DSC) has been proposed.⁷ Type I systems have a crystallization event on the cooling cycle and in Type II systems the crystallization event occurs on the second heating cycle. Type III materials do not display a recrystallization event and so exhibit metastable amorphous phases. This classification can be supported by thermodynamic calculations such as the Hoffmann equation:⁸

$$\Delta G_v^T = \frac{\Delta H_{fus}(T_m - T)T}{T_m^2}$$

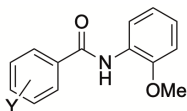
Where ΔH_{fus} = enthalpy of fusion, T_m = melting point, ΔG_v^T = free energy difference between amorphous and crystalline phases at temperature T . This approach assumes the heat capacity of each of the two phases is independent of temperature. The larger the ΔG_v^T the greater the driving force for crystallization. While this analysis gives an insight into thermody-

amic driving force, kinetic factors also contribute to amorphous stability.

Studies into the amorphization of molecular systems for pharmaceutical applications have been a focus of interest owing to the associated practical implications. Most amorphous pharmaceuticals are created as dispersed mixtures on amorphous phases such as polymers and so many studies focus on the stability of such mixtures rather than the individual components.⁹ Studies on pure compounds have generally investigated single compounds or collections of common pharmaceutical ingredients with few chemical structural relationships. For example, machine learning has been applied to 136 compounds to predict crystallization classifications with an accuracy of ~85%.¹⁰ However, these predictions do not reveal the underlying reasons for the different behaviors. A set of twelve related diarylamines¹¹ has been investigated highlighting the entropy of fusion as an identifying factor between good and poor glass-formers with impacts on both thermodynamic and kinetic factors (a correlation with the melt viscosity). However, there is still a lack of insight into the interplay of chemical and crystallographic structure on the resulting stability of amorphous phases, limiting the ability to design and create new phases with useful amorphous properties. Thus, further studies into families of related compounds are required to generate the necessary information.

Benzanilides are frequently studied molecules as models for pharmaceutical materials and the impact of functional groups on crystal packing motifs.¹² The nature of their amorphous phase has been rarely studied and so a set of chemically related 2-methoxybenzanilides (**2MeOBZ-Y**, Scheme 1) have been synthesized and their crystal structures and thermal behavior investigated. The common molecular framework allows for both isostructural crystal structures and molecular factors to be identified through the systems. Computational tools have been

used to identify structural and chemical factors that control the observed behavior.



Y = H, 3-F, 4-F, 3-Cl, 4-Cl, 3-Br, 4-Br, 3-I, 4-I, 3-Me, 4-Me, 3-OMe, 4-OMe, 3-CF₃, 4-CF₃, 3-NO₂, 4-NO₂

Scheme 1. Chemical structure of benzanilides (2MeOBZ-Y) studied.

METHODOLOGY

Synthesis of 2-methoxybenzanilides

Benzanilides of general structure 2-CH₃OC₆H₄NHCOC₆H₄Y; Y = H, CH₃, F, Cl, Br, OCH₃, NO₂ and CF₃ were prepared by condensation of 2-methoxyaniline, CH₃C₆H₄NH₂ with the requisite substituted benzoyl chloride, YC₆H₄COCl, in the presence of an acid scavenger [(C₂H₅)₃N] in cold dichloromethane solution, as illustrated by the specific example described below for 2-CH₃OC₆H₄NHCOC₆H₄(4)CH₃.

All the condensations were done in a fume cupboard, typically at or near ambient temperature, though cooling of the reaction mixture in cold water was sometimes necessary. Most reactions were complete within 1 to 3 hours, but it was generally convenient to leave the reaction mixture stirring overnight before employing the standard workup on the following working day. However, the progress of the reaction was readily monitored by tlc (on SiO₂, eluting with petroleum ether and ethyl acetate, typically in the ratio 2 : 1). The R_f of the substituted benzoyl chloride was usually much greater than that of the more basic benzanilide. It was most economical to employ the cheaper reactant (usually, but not always, the substituted benzoyl chloride) in slight excess (typically about 5%).

Preparation of 2-CH₃OC₆H₄NHCOC₆H₄(4)CH₃.

A solution of 4-methylbenzoyl chloride (1.61 g, 10.4 mmol) in dichloromethane (20 ml) was added drop by drop from a pressure equalizing dropping funnel during 20 minutes to a magnetically stirred solution of 2-methoxyaniline (1.02 g, 8.00 mmol) in dichloromethane (30 ml) containing triethylamine (2.47 g, 24.4 mmol) in a three necked round bottomed flask under a nitrogen atmosphere. Stirring was continued overnight. The reaction mixture was poured into water (100 ml), the organic phase was separated and the aqueous phase was extracted with dichloromethane (3 x 30 ml). The combined organic phases were washed sequentially with aqueous sodium carbonate solution (10% w/v, 20 ml) and dilute hydrochloric acid (2M, 20 ml), dried (MgSO₄), filtered and rotary evaporated to constant mass, with final removal of residual solvent at rotary pump pressure, to give a pale pink solid (2.35 g, 9.73 mmol, 97.6%). Recrystallisation from ethanol/water gave 4-methylbenzoyl-2-methoxyanilide as almost colorless crystals with a faint pink tinge (mpt. 75-6 °C, 1.77 g, 7.34 mmol, 73.5%).

IR Spectroscopy

IR spectra were obtained on a PerkinElmer Spectrum 100 instrument with a UATR attachment (PerkinElmer, USA). Data were acquired between 4000 and 650 cm⁻¹ with a spectral

resolution of 1 cm⁻¹ using 16 scans. Background data were acquired prior to analysis under the same conditions to allow subtraction from the sample data.

Raman Spectroscopy

Raman spectra were acquired using a Renishaw InVia micro-Raman spectrometer (Renishaw, UK) by focusing a suitable crystal of each sample under the x100 (0.95 N_A) lens and exposing to 514 nm excitation from a Laser Physics 50 mW laser attenuated to 10% power using the onboard neutral density filters. Spectra were acquired between 3400 and 100 cm⁻¹ with a spectral resolution of 1 cm⁻¹ using 2 averaged accumulations of 10 second exposure each.

Samples of selected amorphous materials were prepared by melting (*ca.* 2 mg) in a DSC pan placed on a hot plate set to the melting temperature of the compound (determined by DSC) before quench cooling by immediately plunging into liquid nitrogen. The samples were analyzed immediately in the same manner as the crystalline samples.

Thermal Analysis

DSC data were collected using a TA instruments Q2000 equipped with a RCS90 cooling system. Samples (*ca.* 5 mg) were weighed accurately to T-zero aluminum pans and subjected to heat/cool/reheat cycles (reference pan of the same type). The initial heating cycle was performed at 10 °C/min from ambient to 20 °C above the melting temperature of the sample, before cooling to -50 °C at 10 °C/min. The final reheat cycle was performed at 10 °C/min to the same temperature as the first cycle.

Single Crystal X-ray Diffraction

Suitable single crystals of each sample were grown by slow evaporation. Data were collected on a Bruker APEX-II CCD diffractometer. The crystals were kept at 100 K during data collection. Using Olex2,¹³ the structure was solved with the SHELXT¹⁴ structure solution program using Intrinsic Phasing and refined with the SHELXL¹⁵ refinement package using least squares minimization.

Powder X-ray Diffraction

All PXRD data were collected in Bragg-Brentano reflection geometry on a Bruker D8 diffractometer with a Lynxeye detector using X-rays generated from Cu K_α (λ = 1.5418 Å) source. Collections were over the range 5 – 30°/2θ with a step size of 0.02° for a total of 3 minutes.

Computational Methods

Lattice energies of the determined crystal structures were calculated using CASTEP¹⁶ through the Materials Studio interface. The energies were evaluated using the PBE functional with TS dispersion correction,¹⁷ the on-the-fly-generated ultra-soft pseudopotential was used as the basis set.¹⁸ The energy frameworks for each structure were evaluated using CrystalExplorer¹⁹ and calculated at the DFT level (CE-BLYP/36-31G(d,p) except for I containing system CE-HF/3-21G level). Isolated dimers were extracted from the crystal structures and the hydrogen positions optimized in orca²⁰ at the DFT level with the PBEh-3c method²¹ before final evaluation with B2PLYP-D3/def2-QZVPP calculations.²² Crystal structure predictions were carried out using polymorph predictor in Materials Studio with the COMPASSIII forcefield.²³

RESULTS AND DISCUSSION

Crystal Structure Analysis

Single crystal structure determination was carried out on all samples with suitable crystals (Table S1). The **2MeOBZ-Y** systems with Y = H, 3-Cl, 3-Br, 3-I, 3-CF₃, 4-CF₃, 4-NO₂ all display a N-H...O=C H-bond amide chain as the dominant hydrogen bonding interaction. The Y = 4-Cl, 4-Br, 4-I, 4-Me and 3-NO₂ systems lack any strong hydrogen bonding interactions and are based on π ... π stacking interactions. This difference in hydrogen bonding is reflected in the position of the NH and CO stretches in the IR spectra of the compounds. Those featuring the hydrogen bond appear at lower wavenumbers than those without the hydrogen bonding (Table 1). This shift allows for identification of bonding with these systems where single crystal determination was not possible (e.g. Y = 3-F, 4-F, 3-OMe, 3-Me).

Table 1 IR peak positions for NH and CO stretches in selected 2MeOBZ-Y compounds.

Y	$\nu_{\text{NH}}/\text{cm}^{-1}$	$\nu_{\text{CO}}/\text{cm}^{-1}$
H	3237	1638
3-F	3305	1647
4-F	3320	1649
3-Cl	3313	1645
3-Br	3312	1646
3-I	3301	1644
3-Me	3315	1651
3-CF ₃	3306	1647
4-CF ₃	3341	1660
3-OMe	3324	1660
4-OMe	3347	1655
4-NO ₂	3319	1666
4-Cl	3412	1665
4-Br	3409	1664
4-I	3404	1662
4-Me	3424	1660
3-NO ₂	3412	1672

2MeOBZ-H crystallizes as a $Z' = 2$ system with both molecules in a twisted conformation ($\tau_1 = -66, 68^\circ$; $\tau_2 = -156, 164^\circ$) in a monoclinic Pn cell. The NH...O=C bond forms a 1-D chain along the (101) direction. These are linked in to 2-D sheets and the final 3-D structure by weaker CH...OMe H-bonds (Figure 1).

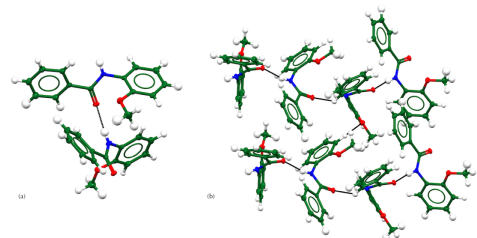


Figure 1 (a) H-bond formed between the symmetry independent molecules in the crystal structure of **2MeOBZ-H**, (b) formation of

2-D sheet through interlinking of two H-bonded chain by weaker CH...O H-bond.

2MeOBZ-Y with Y = 3-Cl and 3-Br are isostructural with a $Z' = 1$ monoclinic $P2_1/n$ unit cell. The NH...O=C H-bond forms a translational chain along the (010) direction, pairs of which form a ladder structure through $R_2^2(8)$ motif formed by CH...OMe bonds (Figure 2a). These ladders are held into a layer structure by weak CH...O=C bonds (Figure 2b). The final 3-D structure forms through Hal...Hal interactions stacking these sheets in a herring bone style.

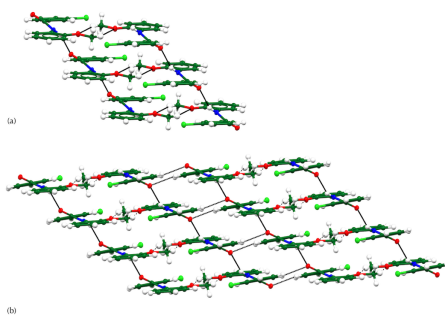


Figure 2 (a) Formation of 1-D ladder in **2MeOBZ-3Cl**, (b) extension of ladders into 2-D sheet by CH...O H-bonds.

2MeOBZ-3I forms a $Z' = 1$ monoclinic $P2_1/c$ unit cell. It is structurally related to **2MeOBZ-3Cl/Br** with a match of 15/30 molecules due to the 1-D ladder structure (Figure 3a). However, the ladders are linked through π ... π interactions generated by the glide plane rather than the 2_1 screw axis to form the final structure (Figure 3b).

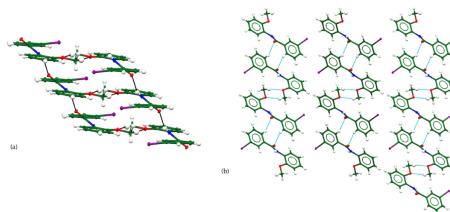


Figure 3 (a) Formation of 1-D ladder in **2MeOBZ-3I**, (b) stacking of sheets into final structure by weaker bonds.

2MeOBZ-3CF₃ has a $Z' = 2$ monoclinic $P2_1/c$ unit cell. The two symmetry independent molecules form separate 1-D translation chains through NH...O=C H-bonds which are linked through weak CH...F bonds (Figure 4a). These structures then form the final 3-D structure through a range of weaker CH...O bonds (Figure 4b).

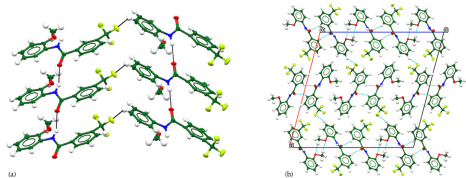


Figure 4 (a) Packing of symmetry independent molecules into 1-D ladder, (b) crystal packing viewed down the *b*-axis for **2MeOBZ-3CF₃**.

2MeOBZ-3NO₂ packs in a $Z' = 2$ *P* *1* triclinic unit cell. One set of symmetry independent molecules forms close dimers through charge transfer interaction between the MeO and NO₂ group which then stack through further $\pi \dots \pi$ interactions (Figure 5). The second molecule also forms a CT stack but with a greater N...O distance present (Figure 5). These stacks then link through CH...O₂N H-bonds forming the final 3-D structure.

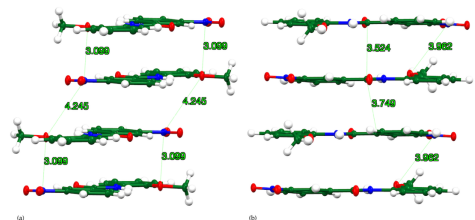


Figure 5 Stacks of **2MeOBZ-3NO₂** molecules formed by two symmetry independent molecules. N...O and close contact distances in Å are shown.

2MeOBZ-Y with Y = 4-Cl, 4-Br and 4-I are all isostructural with a $Z' = 1$ triclinic *P* *1* unit cell. There are no strong H-bonds present and instead 2-D sheets are formed through weaker CH...O bonds (Figure 6a). A combination of $\pi \dots \pi$ stacking and Hal...Hal bonds constructs the final 3-D structure (Figure 6b).

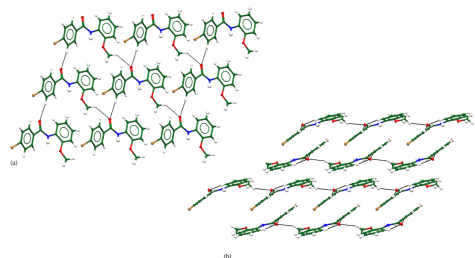


Figure 6 (a) Formation of 2-D sheet in **2MeOBZ-4Br** through weak H-bonds, (b) stacking of sheets into 3-D structure.

2MeOBZ-4Me has structural similarities to the 4-Cl isostructural set with no strong H-bonds present and the same 1-D ladder structure present (Figure 7a). However, the ladders are linked by weak CH...O interactions into stepped sheets,

which are then interlaced together by $\pi \dots \pi$ stacking to give the final 3-D structure (Figure 7b).

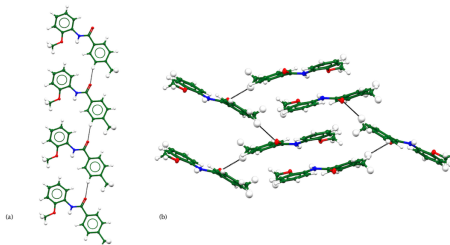


Figure 7 (a) 1-D chain formed in **2MeOBZ-4Me**, (b) interlaced stepped sheets formed by weaker CH...O and $\pi \dots \pi$ interactions.

2MeOBZ-4NO₂ forms a crystal with a $Z' = 1$ monoclinic *P*2₁/*n* unit cell, with a 1-D NH...O=C chain. However, this structure is formed by the glide plane allowing for the overlap of the NO₂ and OMe groups and associated charge transfer interaction ($\pi \dots \pi$). These chains are linked through weaker CH...O interactions into the final 3-D layered structure.

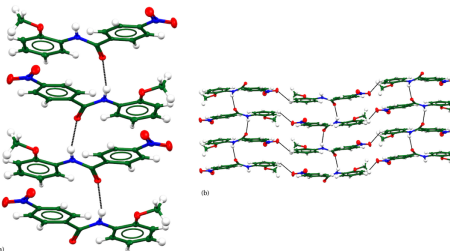


Figure 8 (a) 1-D chain formed by NH...O=C bond in **2MeOBZ-4NO₂**, (b) packing of chains into final 3-D structure.

2MeOBZ-4CF₃ has a $Z' = 1$ orthorhombic *Pna*2₁ unit cell, with a NH...O=C translation chain running in the (001) direction. The chains form a crinkled sheet through CH...F interactions, which are stacked together by CH... π and CH...F interactions to form the final 3-D structure.

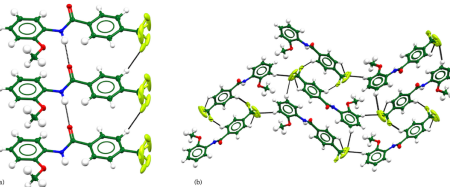


Figure 9 (a) 1-D formed by NH...O=C H-bond in **2MeOBZ-4CF₃**, (b) resulting packing of chains into final 3-D structure.

Thermal Analysis

All the samples were analyzed by heat/cool/heat DSC cycles and classified as either Type I, II or III, while the value of ΔG_f° at 298 K was determined for each system (Table 2, Figures S1 – S17).

Table 2 Summary of thermal properties of 2MeOBZ-Y systems.

Y	Thermal Type	T_m /°C	$\Delta_{fus}H$ /kJ mol ⁻¹	$\Delta_{fus}S$ /J mol ⁻¹ K ⁻¹	ΔG_p^{298K} /kJ mol ⁻¹
H	III	64.3	21.1	62.5	-2.17
3-F	III	58.2	22.1	66.6	-1.99
4-F	III	92.3	28.4	77.7	-4.27
3-Me	III	63.1	29.6	87.9	-2.97
3-CF ₃	III	56.4	26.5	80.3	-2.28
3-OMe	III	50.4	22.0	68.1	-1.59
4-OMe	III	97.1	32.9	88.7	-5.15
3-Cl	II	100.4	33.2	88.9	-5.35
3-Br	II	112.9	36.6	94.6	-6.42
3-I*	II	107.5 112.6	30.6 16.6	80.5 42.9	-5.02 -2.91
4-NO ₂	II/I	146.6	34.0	80.9	-6.99
4-Cl	I	124.9	32.3	81.2	-6.08
4-Br	I	141.6	40.4	97.4	-8.16
4-I	I	134.5	31.0	76.0	-6.09
4-Me	I	74.1	22.3	64.2	-2.70
4-CF ₃	I	109.1	29.8	78.0	-5.12
3-NO ₂	I	145.4	35.3	84.2	-7.22

*=second polymorph formed on second heating cycle.

For most systems, the thermodynamic behavior agrees with the empirical classification with low values of free energy corresponding to good glass-forming systems. However, there are some anomalous values, with Y = 4-Me showing comparable values to Type III systems but exhibiting Type I behavior. To investigate whether the chemical structure had a direct effect on the behavior the free energy values were plotted against the Hammett σ -constants²⁴ for the different substituents (Figure 10).

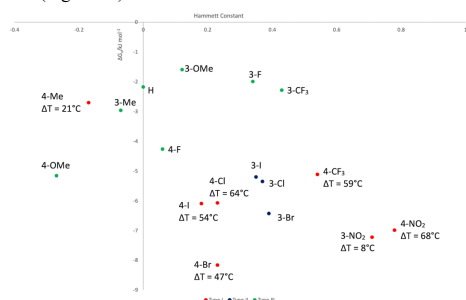


Figure 10 Plot of ΔG_p^{298K} against the Hammett σ -constant of the different substituents. Type I systems (red), Type II (blue) and Type III (green). For Type I systems the temperature difference between the melting point and recrystallisation point are given.

While there is a clustering to the data with a suggestion of electron-withdrawing groups favoring Type I and electron-

donating Type III, the chemical structure is not a definite dominating factor. The isostructural sets have similar properties and are closely clustered, reflecting the similar chemical properties of the Cl/Br/I substituents. **2MeOBZ-4Me** is clearly anomalous, along with **2MeOBZ-4NO₂** which shows differing behavior in different samples (Figure S17). **2MeOBZ-4Me** has the highest driving force of the Type III systems suggesting a kinetic factor in the behavior of this case. To investigate the structural changes that occur during the conversion process, Raman spectroscopy was undertaken on crystalline and amorphous phases.

Raman Spectroscopy of Amorphous/Crystalline Phases

For selected samples (Y = 3-NO₂, 4-Me, 4-I, 4-NO₂, 4-OMe and 4-Br), Raman spectra were collected for both the crystalline and amorphous phases generated by liquid nitrogen quenching. In the case of **2MeOBZ-3NO₂**, no amorphous phase could be obtained with recrystallization occurring upon removal from the hot plate.

2MeOBZ-4Me and **2MeOBZ-4I** show no change in the peak positions between the two phases although the amorphous phase has broader peaks (Figure 11). This suggests there is little change in the local environment about the molecules. In contrast, the spectra for Y = 4-NO₂, 4-OMe (Figure 12) all show clear shifts in the C=O stretching band, which moves to higher wavenumber. In the case of **2MeOBZ-3Br**, the sample recrystallized during subsequent Raman analysis confirming that the peak shifts do correlate with the change in phase (Figure 13). For the amorphous phases, the new peak position now matches the location in crystal systems which lack the NH...O=C H-bond. These results indicate that in the amorphous phases the stronger H-bonding between the molecules is lost. Thus, those crystals which lack such a bond (Y = 4-Cl, 4-Br, 4-I, 4-Me, 3-NO₂, all Type I) can more rapidly recrystallize, compared to those systems featuring NH...O=C bond (Y = H, 3-F, 4-F, 3-Me, 4-OMe, 3-CF₃ all Type III, 3-Cl, 3-Br, 3-I are type II). **2MeOBZ-4NO₂** does feature a NH...O=C H-bond but also has a large ΔG_p^{298K} suggesting that the thermodynamic driving force can overcome the kinetic factors in this case. However, these properties are closely balanced as shown by the sample variability in behavior with different samples classified as either Type I or II.

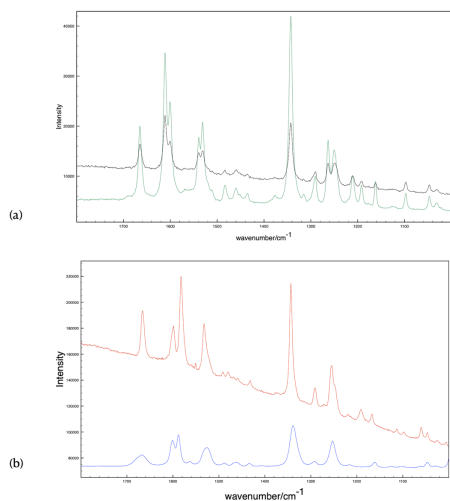


Figure 11 Comparison of Raman spectra in the range 1800 – 1000 cm^{-1} for (a) **2MeOBZ-4Me** (crystalline phase green line, amorphous black line) and (b) **2MeOBZ-4I** (crystalline phase red line, amorphous phase blue line).

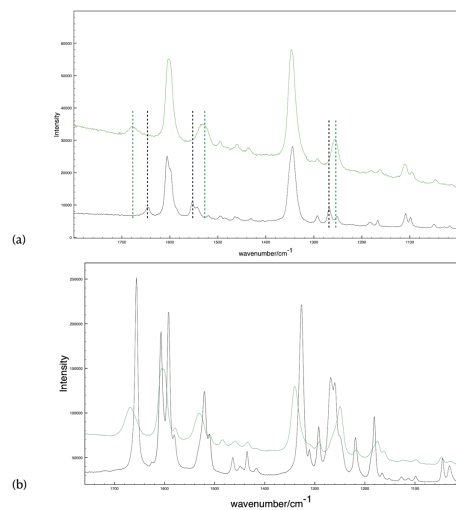


Figure 12 Comparison of Raman spectra in the range 1800 – 1000 cm^{-1} for (a) **2MeOBZ-4NO₂** (crystalline phase green line, amorphous black line) and (b) **2MeOBZ-4OMe** (crystalline phase black line, amorphous phase green line).

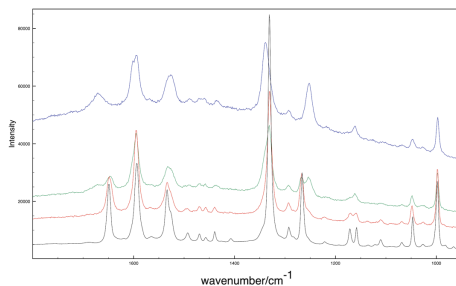


Figure 13 Comparison of Raman spectra in the range 1800 – 1000 cm^{-1} for **2MeOBZ-3Br** for crystalline (black line) and amorphous (blue line) samples. Subsequent collections captured mixed amorphous/crystalline sample (green) and recrystallized sample (red line).

Energetic Analysis

The lattice energies of crystal structures of the samples determined were calculated at the DFT level using CASTEP (Table 3). These show little variation between the materials confirming that the differences in behavior between the phases is not dependent on the overall crystal energy but rather specific interactions. The energy framework for each system was calculated in CrystalExplorer, with each system displaying a strong 1-D chain interaction with weaker interactions between these chains (Table 3).

Table 3 Energetics for molecular crystals

System	Lattice Energy [§] kJ mol^{-1}	Strongest Intermolecular Interactions [†] / kJ mol^{-1}
2MeOBZ	-172	NH...O=C: -50.6/-61.2 interchain: -23.2/-21.3
2MeOBZ-3CF₃	-173	NH...O=C: -56.9 interchain: -28.2
2MeOBZ-4OMe	-187	NH...O=C: -46.6 interchain: -19.7
2MeOBZ-3Cl	-172	NH...O=C: -51.3 interchain: -17.1
2MeOBZ-3Br	-172	NH...O=C: -54.1 interchain: -7.8
2MeOBZ-3I	-179	NH...O=C: -57.2 interchain: -17.2
2MeOBZ-4NO₂	-185	NH...O=C: -58.6 interchain: -12.5
2MeOBZ-4Cl	-172	π stack: -57.1 interchain: -14.1
2MeOBZ-4Br	-171	π stack: -60.7 interchain: -15.7
2MeOBZ-4I	-175	π stack: -62.7 interchain: -32.5
2MeOBZ-4Me	-175	π stack: -36.1

		interchain: -31.9, -24.1
2MeOBZ-4CF₃	-173	NH...O=C: -55.9 interchain: -30.5, -23.3
2MeOBZ-3NO₂	-191	π stack: -80.4/-60.1 interchain: -12.7

§Calculated CASTEP PBE-TS/OTFG ultrasoft potential;
†calculated CE-B3LYP-D3/6-31(d,p) except 1 CE-HF/3-21G

2MeOBZ-4Me shows the weakest dominant interaction; however, it has more secondary interactions of higher strength than the other systems. These lead to an interlaced structure that does not have room to significantly alter upon melting (Figure 14). This supports the lack of change observed in the Raman spectra of the amorphous phase. Therefore, while **2MeOBZ-4Me** thermodynamically would be expected to be a Type III system, the kinetics enforce the Type I behavior.

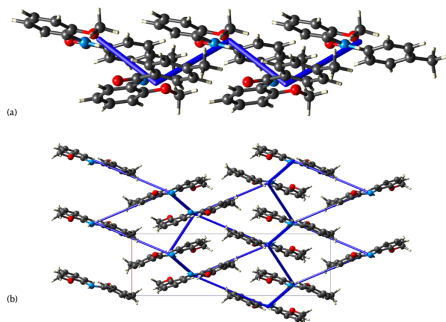


Figure 14 (a) Formation of 1-D chain through the strongest intermolecular interaction in **2MeOBZ-4Me**, (b) interlaced packing of the chains into the final 3-D structure showing the 2nd and 3rd strongest interactions.

The lack of the NH...O=C H-bond appears to be an important factor in the kinetics of the Type I/III systems as the absence of this bond prevents rapid recrystallisation. However, it is not yet clear why the systems do not have this interaction since the NH is not forming a competing H-bond. For the halogenated systems and 3-NO₂ the alternative π -stack interaction is lower in energy compared to other H-bonded interactions and so offers sufficient stabilization without the need for such a hydrogen bond.

For **2MeOBZ-4Me**, the energy difference between the crystal dimer and an optimized H-bonded dimer was -6.14 kJ mol⁻¹ in favor of the H-bonded dimer. This finding suggests that, in this case, other packing interactions are strong enough to compensate for the lack of H-bonding. A polymorph prediction study was undertaken for this compound to investigate the energy landscape of potential polymorphs (Figure 15). The lowest energy structures were isostructural to the known crystal structure (with a shift in the molecular conformation, Figure 16) and all lack the NH...O=C hydrogen bond. However, low energy structures with this interaction are predicted within 3 kJ mol⁻¹ for the known structure. Thus, in principle, this system may be polymorphic and exhibit differences in the crystallization behavior, but the strength of other potential

interactions can compensate for the lack of the strongest potential interaction.

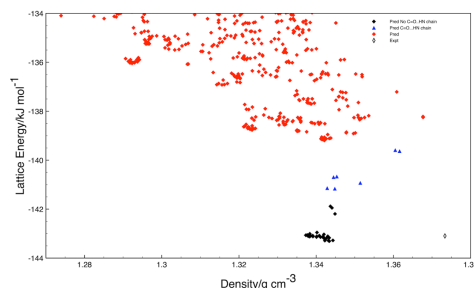


Figure 15 Predicted energy landscape for **2MeOBZ-4Me**. Lowest energy systems without NH...O=C bond (black diamonds), with NH...O=C (blue triangles) and experimental structure (open diamond) are highlighted. Remaining structures are in red.

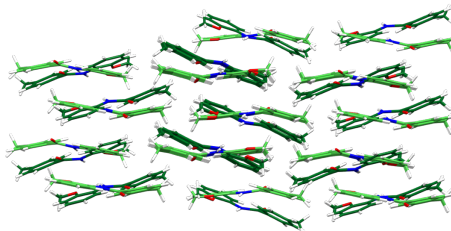


Figure 16 Overlay of lowest energy predicted structure (dark green) with the experimental structure (light green).

Dimer calculations for **2MeOBZ-3NO₂** show that the observed dimer is favored by 36.76 kJ mol⁻¹ over an alternative H-bonded dimer, while for **2MeOBZ-4NO₂** the H-bond dimer in the crystal structure is lower in energy by 25.01 kJ mol⁻¹ compared to the optimized charge transfer also present in the crystal. However, analysis of the geometry of the dimer shows that there is still a CT interaction in the H-bonded case (Figure 17) stabilizing the overall interaction. This analysis shows that the relative geometry of the functional group is important to allow for generation of complementary interactions, which presumably permits more rapid regeneration of the crystalline H-bond after melting.

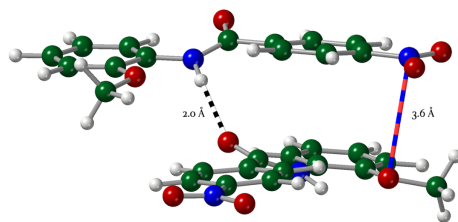


Figure 17 H-bonded dimer from **2MeOBZ-4NO₂** showing close N...O contact corresponding to CT interaction.

For most systems then, the free energy difference is the dominant contribution to the stabilization of the crystalline phase. For most of the Type I and III systems, the kinetics of the bond breaking process align with the thermodynamics; consequently, systems without a NH...O=C H-bond generally crystallize rapidly owing to energetic factors; in contrast, systems with such a bond prefer to form metastable glasses. However, some exceptions occur, where the kinetics overcome the expected energetic outcome, such as **2MeOBZ-4Me** in which crystallization is energetically unfavorable, but the limited structural changes between the crystalline and melt phases accelerate crystallization.

CONCLUSION

The creation of metastable amorphous phases is an important objective for the development of novel functional materials. The interplay between chemical and crystal structure in stabilizing the amorphous phase can be subtle. The set of benzanilides studied displays the full range of amorphous behavior with only small chemical shifts on a base framework. The introduction of a methoxy group stabilizes the stacking interactions with electron acceptor group over the otherwise dominant amide hydrogen bonding. This in turn results in a reduction in the level of change that occurs upon melting and so reduces the stability of the amorphous phase. The underlying energetic difference between the crystalline and amorphous phases are generally matched by these kinetic factors but sometimes the kinetic factors dominate the process as shown by **2MeOBZ-4Me**, which has a predictable lack of a hydrogen bonding interaction but low energetic stability. The use of computational tools to understand the potential interactions present and energetic distribution in the crystalline phases gives an initial route to identify potential amorphous phases.

This work highlights the subtle interplay of many structural and energetic factors in the creation of amorphous of extended stability, which requires further investigation into both creation of amorphous phases and the longer-term stability and recrystallisation kinetics.

ASSOCIATED CONTENT

Supporting Information

The Supporting Information is available free of charge on the ACS Publications website.

Details of crystal structure determination, DSC traces for each sample (pdf).

The crystal [structures](#) in the paper have been deposited with the CCDC. CCDC Numbers 2296848-2296858 contain the supplementary crystallographic data for this paper. These data can be obtained free of charge via www.ccdc.cam.ac.uk/data_request/cif, or by emailing data_request@ccdc.cam.ac.uk, or by contacting The Cambridge Crystallographic Data Centre, 12 Union Road, Cambridge CB2 1EZ, UK; fax: +44 1223 336033.

AUTHOR INFORMATION

Corresponding Author

*e-mail c.seaton@bradford.ac.uk

Author Contributions

The manuscript was written through contributions of all authors. All authors have given approval to the final version of the manuscript.

REFERENCES

1. Cruz-Cabeza, A. J.; Reutzel-Edens, S. M.; Bernstein, J. Facts and Fictions about Polymorphism. *Chem. Soc. Rev.* **2015**, *44* (23), 8619–8635.
2. Gunawardana, C. A.; Aakeröy, C. B. Co-Crystal Synthesis: Fact, Fancy, and Great Expectations. *Chem. Commun.* **2018**, *54* (100), 14047–14060; Cruz-Cabeza, A. J.; Lestari, M.; Lusi, M. Cocystals Help Break the “Rules” of Isostructurality: Solid Solutions and Polymorphism in the Malic/Tartaric Acid System. *Cryst. Growth Des.* **2018**, *18* (2), 855–863; Clarke, H. D.; Arora, K. K.; Bass, H.; Kavuru, P.; Ong, T. T.; Pujari, T.; Wojtas, L.; Zaworotko, M. J. Structure–Stability Relationships in Cocystal Hydrates: Does the Promiscuity of Water Make Crystalline Hydrates the Nemesis of Crystal Engineering? *Cryst. Growth Des.* **2010**, *10* (5), 2152–2167.
3. Laitinen, R.; Löbmann, K.; Strachan, C. J.; Grohgan, H.; Rades, T. Emerging Trends in the Stabilization of Amorphous Drugs. *Int. J. Pharm.* **2013**, *453* (1), 65–79.
4. Johari, G. P.; Shanker, R. M. On the Solubility Advantage of a Pharmaceutical’s Glassy State over the Crystal State, and of Its Crystal Polymorphs. *Thermochim. Acta* **2014**, *598*, 16–27.
5. Hasebe, M.; Musumeci, D.; Yu, L. Fast Surface Crystallization of Molecular Glasses: Creation of Depletion Zones by Surface Diffusion and Crystallization Flux. *J. Phys. Chem. B* **2015**, *119* (7), 3304–3311.
6. Liu, J.; Liu, G.; Song, Z.; Kaltenecker, M.; Moraes, L. S. de; Gopi, E.; Napolitano, S.; Geerts, Y. H. Memory Effect and Crystallization of (R, S)-2-Chloromandelic Acid Glass. *J. Phys. Chem. B* **2021**, *125* (48), 13339–13347; Sibik, J.; Sargent, M. J.; Franklin, M.; Zeitler, J. A. Crystallization and Phase Changes in Paracetamol from the Amorphous Solid to the Liquid Phase. *Mol. Pharmaceutics* **2014**, *11* (4), 1326–1334; Baird, J. A.; Santiago-Quinonez, D.; Rinaldi, C.; Taylor, L. S. Role of Viscosity in Influencing the Glass-Forming Ability of Organic Molecules from the Undercooled Melt State. *Pharm. Res.* **2012**, *29* (1), 271–284; Wang, B.; Biesold, G. M.; Zhang, M.; Lin, Z. Amorphous Inorganic Semiconductors for the Development of Solar Cell, Photoelectrocatalytic and Photocatalytic Applications. *Chem. Soc. Rev.* **2021**, *50* (12), 6914–6949.
7. Baird, J. A.; Eerdenbrugh, B. V.; Taylor, L. S. A Classification System to Assess the Crystallization Tendency of Organic Molecules from Undercooled Melts. *J. Pharm. Sci.* **2010**, *99* (9), 3787–3806.
8. Bhugra, C.; Pikal, M. J. Role of Thermodynamic, Molecular, and Kinetic Factors in Crystallization from the Amorphous State. *J. Pharm. Sci.* **2008**, *97* (4), 1329–1349.
9. Nie, H.; Mo, H.; Zhang, M.; Song, Y.; Fang, K.; Taylor, L. S.; Li, T.; Byrn, S. R. Investigating the Interaction Pattern and Structural Elements of a Drug–Polymer Complex at the Molecular Level. *Mol. Pharmaceutics* **2015**, *12* (7), 2459–2468.
10. Barnard, T.; Sosso, G. C. Combining Machine Learning and Molecular Simulations to Predict the Stability of Amorphous Drugs. *J. Chem. Phys.* **2023**, *159* (1), 014503.
11. Kalra, A.; Luner, P.; Taylor, L. S.; Byrn, S. R.; Li, T. Gaining Thermodynamic Insight from Distinct Glass Formation Kinetics of Structurally Similar Organic Compounds. *J. Pharm. Sci.* **2018**, *107* (1), 192–202.
12. Wardell, J. L.; Low, J. N.; Skakle, J. M. S.; Glidewell, C. Isomeric N-(iodophenyl)Nitrobenzamides Form Different Three-Dimensional Framework Structures. *Acta Crystallogr Sect B Struct Sci* **2006**, *62* (5), 931–943; Nayak, S. K.; Reddy, M. K.; Row, T. N. G.; Chopra, D. Role of Hetero-Halogen (F...X, X = Cl, Br, and I) or Homo-Halogen (X...X, X = F, Cl, Br, and I) Interactions in Substituted Benzanilides. *Cryst. Growth Des.* **2011**, *11* (5), 1578–1596; Zipp, C. F.; Dirr, H. W.; Fernandes, M. A.; Marques, H. M.; Michael, J. P. Polymorphic Diversity: N-Phenylbenzamide as a Possible Polymorphophore. *Cryst. Growth Des.* **2013**, *13* (8), 3463–3474; Mondal, P. K.; Shukla, R.; Biswas, S.; Chopra, D. Role of Halogen-involved Intermolecular Interactions and Existence of Isostructurality in the Crystal Pack-

- ing of —CF₃ and Halogen (Cl or Br or I) Substituted Benzamides. *Acta Crystallogr. Sect. B* **2018**, *74* (6), 574–591.
13. Dolomanov, O. V.; Bourhis, L. J.; Gildea, R. J.; Howard, J. A. K.; Puschmann, H. OLEX2: A Complete Structure Solution, Refinement and Analysis Program. *J. Appl. Crystallogr.* **2009**, *42* (2), 339–341.
 14. Sheldrick, G. M. SHELXT – Integrated Space-Group and Crystal-Structure Determination. *Acta Crystallogr. Sect. Found. Adv.* **2015**, *71* (Pt 1), 3–8.
 15. Sheldrick, G. M. Crystal Structure Refinement with SHELXL. *Acta Crystallogr. Sect. C Struct. Chem.* **2015**, *71* (1), 3–8.
 16. Clark, S. J.; Segall, M. D.; Pickard, C. J.; Hasnip, P. J.; Probert, M. J.; Refson, K.; Payne, M. C. First Principles Methods Using CASTEP. *Z. Kristall.*, **2005**, *220*, 567–570.
 17. Tkatchenko, A.; Scheffler, M. Accurate Molecular van der Waals Interactions from Ground-State Electron Density and Free-Atom Reference Data. *Phys. Rev. Lett.* **2009**, *102* (7), 073005.
 18. Hohenberg, P.; Kohn, W. Inhomogeneous Electron Gas. *Phys. Rev.* **1964**, *136* (3B), B864–B871; Kohn, W.; Sham, L. J. Self-Consistent Equations Including Exchange and Correlation Effects. *Phys. Rev.* **1965**, *140* (4A), A1133–A1138; Byrd, R. H.; Nocedal, J.; Schnabel, R. B. Representations of Quasi-Newton Matrices and Their Use in Limited Memory Methods. *Math. Prog.* **1994**, *63*, 129–156; Payne, M. C.; Teter, M. P.; Allan, D. C.; Arias, T. A.; Joannopoulos, J. D. Iterative Minimization Techniques for Ab Initio Total-Energy Calculations - Molecular-Dynamics and Conjugate Gradients. *Rev. Mod. Phys.* **1992**, *64*, 1045–1097; Pfommer, B. G.; Côté, M.; Louie, S. G.; Cohen, M. L. Relaxation of Crystals with the Quasi-Newton Method. *J. Comput. Phys.* **1997**, *131* (1), 233–240; McNellis, E. R.; Meyer, J.; Reuter, K. Azobenzene at Coinage Metal Surfaces: Role of Dispersive van der Waals Interactions. *Phys. Rev. B* **2009**, *80*, 205414; Packwood, D.; Kermode, J.; Mones, L.; Bernstein, N.; Woolley, J.; Gould, N.; Ortner, C.; Csányi, G. A Universal Preconditioner for Simulating Condensed Phase Materials. *J. Chem. Phys.* **2016**, *144* (16), 164109.
 19. Spackman, P. R.; Turner, M. J.; McKinnon, J. J.; Wolff, S. K.; Grimwood, D. J.; Jayatilaka, D.; Spackman, M. A. CrystalExplorer: A Program for Hirshfeld Surface Analysis, Visualization and Quantitative Analysis of Molecular Crystals. *J. Appl. Crystallogr.* **2021**, *54* (3), 1006–1011.
 20. Neese, F. Software Update: The ORCA Program System—Version 5.0. *Wiley Interdiscip. Rev. Comput. Mol. Sci.* **2022**.
 21. Grimme S.; Brandenburg, J. G.; Bannwarth, C.; Hansen A. Consistent structures and interactions by density functional theory with small atomic orbital basis sets, *J. Chem. Phys.*, **2015**, *143*(5), 054107. Kruse, H.; Grimme S. A geometrical correction for the inter- and intra-molecular basis set superposition error in Hartree-Fock and density functional theory calculations for large systems, *J. Chem. Phys.*, **2012**, *136*(15), 154101; Grimme, S.; Ehrlich, S.; Goerigk, L. Effect of the Damping Function in Dispersion Corrected Density Functional Theory. *J. Comput. Chem.* **2011**, *32* (7), 1456–1465; Grimme, S.; Antony, J.; Ehrlich, S.; Krieg, H. A Consistent and Accurate Ab Initio Parametrization of Density Functional Dispersion Correction (DFT-D) for the 94 Elements H-Pu. *J. Chem. Phys.* **2010**, *132* (15), 154104; Weigend, F. Accurate Coulomb-Fitting Basis Sets for H to Rn. *Phys. Chem. Chem. Phys.* **2006**, *8* (9), 1057–1065.
 22. Weigend, F.; Ahlrichs, R. Balanced Basis Sets of Split Valence, Triple Zeta Valence and Quadruple Zeta Valence Quality for H to Rn: Design and Assessment of Accuracy. *Phys. Chem. Chem. Phys.* **2005**, *7* (18), 3297–3305; Weigend, F. Accurate Coulomb-Fitting Basis Sets for H to Rn. *Phys. Chem. Chem. Phys.* **2006**, *8* (9), 1057–1065; Hellweg, A.; Hättig, C.; Höfener, S.; Klopffer, W. Optimized Accurate Auxiliary Basis Sets for RI-MP2 and RI-CC2 Calculations for the Atoms Rb to Rn. *Theor. Chem. Acc.* **2007**, *117* (4), 587–597.
 23. Akkermans, R. L. C.; Spenley, N. A.; Robertson, S. H. COMPASS III: Automated Fitting Workflows and Extension to Ionic Liquids. *Mol. Simul.* **2021**, *47* (7), 540–551.
 24. Hansch, Corwin.; Leo, A.; Taft, R. W. A Survey of Hammett Substituent Constants and Resonance and Field Parameters. *Chem. Rev.* **1991**, *91* (2), 165–195.

For Table of Contents use

